Comprehensive properties of passive film formed in simulated pore solution of alkali-activated concrete

Zuquan Jin[1*] , Xia Zhao [2,4*] , Yujiao Du[1], Siyu Yang[3], Danqian Wang[3], Tiejun Zhao[1], Yun Bai[3*]

[1]Cooperative Innovation Center of Engineering Construction and Safety in Shandong Blue Economic Zone, Qingdao University of Technology, Qingdao, China

[2]CAS Key Laboratory of Marine Environmental Corrosion and Bio-fouling, Institute of Oceanology, Chinese Academy of Science, Qingdao, China

[3]Department of Civil, Environmental and Geomatic Engineering, University College London, London, UK

[4]Center for Ocean Mega-Science, Chinese Academy of Sciences, Qingdao, China

*E-mail: jinzuquan@126.com; zx@qdio.ac.cn; yun.bai@ucl.ac.uk

Abstract:

The study on the properties of passive films in alkali-activated slag cement can provide a theoretical basis for the development and application of low-carbon and environmental friendly concrete materials. In this paper, the passivation behaviour of anti-corrosion rebar (AR) and normal reinforcing steel (NR) in sulfur-free simulated pore solutions of alkali-activated slag cement pastes was investigated using electrochemical, microscale techniques and molecular dynamics modelling. Results showed that the formation time, composition and thickness of the passive film were affected by the types of simulated pore solutions. Molecular dynamics further elucidated the reason for difference in the protective ability of passive film in three types of simulated pore solutions. The results of protection capability of two kinds of rebar obtained from molecular dynamics were consistent with those of electrochemical impedance spectroscopy (EIS).

Keywords: passivation; steel bar; alkali-activated; protective ability; molecular dynamics

1. INTRODUCTION

The production of one tonne of Portland cement (PC) consumes 4 GJ of energy and emits nearly 0.85 tons of carbon dioxide to the atmosphere [1]. In China alone, 2.35 billion tonnes of cement were produced in 2019, causing serious environmental problems. Therefore, it is of great

value and significance to find alternative low-carbon cement for the sustainable development of construction industry. Industrial by-products, such as ground granulated blast furnace slag (GGBS), fly ash and silica fume, have much lower embodied CO_2 than PC and, hence, have been widely accepted as partial replacements for PC to meet the sustainability requirements of construction industry [2-4]. Although the current PC standard allows high replacement levels, such as up to 95% GGBS [5], in practice, this may lead to performance degradation, such as low early strength[6], reduced tensile strength and splitting tensile strength[7], and a significant increase in carbonation rate[8], which has attracted industry attention [9].

By contrast, high performance cementitious materials can be formulated using alkaline activators, such as sodium silicate and sodium hydroxide, to active GGBS or fly ash to replace PC, and these materials are generally referred to as alkali-activated cementitious materials (AAM) [10]. Compared to the PC concretes blended with high level industrial by-products, AAM has demonstrated some superior properties. For example, after good design, AAM concrete exhibits lower hydration heat, higher early strength and better resistance to sulfate attacks than PC [11-13]. Extensive research interests have, thus, been generated worldwide in the past to investigate its hydration products, strength and microstructures in order to develop a scientific basis for its industrial application [14]. On the other hand, some other properties directly related to the construction practice have also attracted some attention. For instance, it has been confirmed that the bond strength between reinforcing bar and AAM concrete is better than that with PC[15-16]. Although AAM is known to be more prone to cracking, super absorbent polymer (SAP) and fiber have been shown to be able to improve its crack resistance [17]. Furthermore, numerous experimental results have also indicated that the AAM is a strain-rate sensitive material with its failure modes under impact load similar to those of PC. All these studies have thus indicated that AAM concrete has many potential promising applications [18].

Among various possible applications, AAM is considered to be more suitable for servicing marine environments than PC concrete. Through the good design of mix proportion for alkali-activated materials, the silicon content (Si: Al ratio), alkali content (Na: Al ratio) and water content (L: s ratio) can be improved, so as to refine the pore structure, improve the chloride binding ability, and further strengthen the chloride resistance ability of AAM in marine environment [19-22]. And

increasing the amount of Si in activator would result in a lower total porosity and a finer pore structure[23]. Additionally, Monticelli et al. reported that alkali-activated fly ash mortars could enhance the protection towards the steel bar compared to PC [24]. On the other hand, it has been postulated that the hydration products, such as C-A-S-H and N-A-S-H, as well as the SiO_3^{2-} and AlO^{2-} ions, in AAM could be adsorbed on the passive film of steel bar and, hence, be able to delay the chloride-induced depassivation [25-26]. In addition, the CO_3^{2-} in the pore solution of Na_2CO_3 activated slag was also found to be able to decrease the defects of passive film and, therefore, hinder the pitting corrosion of steel bar [27]. Therefore, it can be deduced that AAM could be a better alternative cementitious material for marine structures where chloride-induced corrosion is the main durability concern. Generally, a protective passive film, composed of iron oxide and hydroxide, forms on the surface of steel rebar in PC, which stabilizes the steel rebar from chloride-induced corrosion. Since the resistance of steel bar to corrosion is believed to be closely related to the properties of the passive film formed in concrete pore solution [28], a good understanding of the passivation mechanisms of steel bar in AAM is important for the durability design of AAM-based structures. Unfortunately, the study on the passivation of steel in AAM is considerably scarce in the literature. Moreover, the protective capacity of passive film could be influenced by the pore solution chemistry of AAM, such as the pH and anions in the AAM pore solutions. In practice, the situation is even more complex since AAM concrete could be designed with similar strength using different activators. Although mechanically this would not generate much difference, the pore solution chemistry could be different. As a result, the passivation of steel bar might be affected. On the other hand, AR has been found to be an effective solution to improve the durability of reinforced concrete in severe marine environment [29-30], because the Cr existing in AR steel matrix could help to produce a protective layer on steel bar, leading to a much improved resistance to chloride-induced corrosion [31]. As a result, the critical chloride value could be significantly enhanced when AR is adopted in reinforced concrete structure. Based on this, it could be deduced that the concrete cover thickness and even concrete compactness required to resist the chloride penetration can be reduced. Hence, the cracking risk of concrete cover and construction difficulty may be decreased, which contributes to a higher cost-efficiency ratio for adopting AAM in reinforced concrete structure. Therefore, it can be concluded that the resistance of AAM-based reinforced concrete to the chloride-induced corrosion not only depends upon the type of chemicals to be employed as activator, but also

relies on the type of steel bar to be used as reinforcement.

Due to the complexity of the composition of AAM pore solution and the difference between simulated pore solution and actual environment [32], the passivation and corrosion behavior of steel bar by pore solution is very different from that of actual concrete. However, regarding the influence of materials and environment on the passivation and depassivation of steel bars, the key information of passivation time, passive film thickness as well as depassivation of steel bars can be quickly obtained by using the simplified simulated pore solution. However, due to the variety and high concentration of ions in alkali activated pore solution, the mechanism of passivation and depassivation is very complex. Among them, the influence of sulfur ion is more complex and needs more systematic and comprehensive research in the future. Therefore, the purpose of this paper is to study the passivation process and passive film performance of NR and AR steel bars in sulfur free simulated pore solution of alkali activated concrete, which can preliminarily provide a set of methods for characterizing the microstructure of the passive film, and some experimental basis for the mix proportion optimization of high durability steel reinforced alkali activated concrete materials.

2 EXPERIMENTAL

2.1 Materials and specimen preparation

2.1.1 preparation of AAM mortars

S95 GGBS (Chinese standard GB/T18046-2008) was used as basic materials, which was activated by alkali, with a mainly chemical composition of (% by weight) 46.34 CaO, 29.05 SiO_2, 12.51 Al_2O_3, 1.3 Fe_2O_3, 5.72 MgO and 1.18 SO_3. The specific surface area and gravity of S95 GGBS is 379m^2/kg and 2.81, respectively. Both NaOH and Na_2SiO_3 were used as alkali activators for S95 GGBS. The Na_2O concentration in the two kinds of activating solutions was 5% by weight of slag. The mortar with Na_2SiO_3 as the activator is called PSS, while the mortar with NaOH as the activator is called PSH. The river sand with a fineness modulus of 2.7 was used as aggregate, and the sand/binder weight ratio was 2.0 for both AAM mortars. Mortar samples with a size of 40×10×160mm^3 were used for pore solution extraction. Given that the chemical composition of

pore solutions in AAM is nearly unchanged from 7 d to 180 d [31], the mortar specimens were all cured for 14 days at (20±3) ℃ and 95% relative humidity and crushed for pore solution extraction.

2.1.2 preparation of the simulated pore solutions

The device and methods of pore solution extraction in this experiment was referred to Wang et al [33]. The pH of the extracted pore solutions were determined using a precision pH meter, and the concentrations of each element were measured by inductively coupled plasma optical emission spectroscopy. The concentration of the elements and pH of pore solutions were listed in Table 1. The chemical composition of extracted pore solution of AAM were dominated by [Na] with the concentrations above 10^4 ppm, and lower concentrations of [K], [Al], [Ca] were observed in the same specimen. And low concentrations of [SO_4^{2-}] and [S^{2-}] were observed in PSS and PSH solutions. Due to the limited amount of pore solution extracted from mortar as well as the complex influence of anions, such as [SO_4^{2-}] and [S^{2-}], on the passivation and depassivation process of reinforcement, in this study, sulfur free simulated pore solution was prepared according to the composition of the extracted pore solution in Table 1. Meanwhile, an alkaline solution with pH and chemical composition consistent with those previously reported, was used as simulated pore solution of PC mortars [34].

Table 1 Chemical elements and pH of the pore solutions extracted from AAM mortars (ppm)

Mortars	Activator	Al	Ca	Fe	K	Na	P	SO_4^{2-}	S^{2-}	pH
PSS	Na_2SiO_3	1.15×10^2	10.5	2.74	2.83×10^2	1.42×10^4	13.44	3.55×10^3	6.72×10^3	13.03
PSH	NaOH	6.07×10^2	1.67	<1	1.77×10^3	3.67×10^4	10.21	2.69×10^3	8.64×10^3	13.53
PC	/	/	8.98×10^2	/	2.25×10^4	4.60×10^3	/	/	/	13.35

2.1.3 Preparation of WE

The working electrode (WE) in the electrochemical tests were made from either AR or NR bars with a diameter of 10 mm and a length of 3 mm, respectively. Table 2 presents the chemical composition of AR and NR. A copper wire lead was soldered to one end of the WE, whilst the other end was exposed as working surface. The rest of the WE was then sealed by epoxy resin. The working surface was sequentially polished by SiC water polishing papers with grits of 400-1500#. Finally, the WE was ultrasonically degreased in acetone, washed in distilled water, and then dried at room temperature.

Table 2 Chemical compositions of steel bar (%)

Type	Chemical compositions								
	Fe	C	Si	Mn	P	S	V	Cr	Mo
AR	Bal.	0.01	0.49	1.49	0.01	0.01	0.06	10.36	1.16
NR	Bal.	0.22	0.53	1.44	0.02	0.02	0.04	-	-

2.2 Electrochemical experiments

Electrochemical experiments were conducted with a classical three electrode configuration. The rebar acted as the WE with a platinum foil of 2.0 cm×2.0 cm as the counter electrode and a saturated calomel electrode with a Luggin capillary as the reference electrode. The electrochemical measurements were performed using a Princeton Versa STAT 3 potentiostat/galvanostat (Princeton Applied Research, Oak Ridge, United States) at (23±2)℃. EIS measurements were determined in the frequency range from 100 kHz to 10 mHz at steady open-circuit potential with a disturbance amplitude of 10 mV. The EIS data were analysed by ZsimpWin software (Echem software, USA). All the tests were carried out in triplicate for each sample.

2.3 Characterization of Chemical composite and microstructure of passive film

X-Ray photoelectron spectroscopy (XPS) with a non-monochromatic Al Kα X-ray source was used to analyse the passive film developed on the surface of the steel bar in simulated pore solutions. Spectra of Fe 2p and Cr 2p were recorded. The argon ion sputtering was used to obtain the chemical composition of passive film information at different depths. Before each scan, ionized argon ion beam etched the sample layer at a sputtering speed of 0.2 nm/s. In this way, the depth profile could obtained for the passive film. The software used for deconvolution of XPS spectra is XPS Peak Fit.

The microstructure of passive film on the steel bar surface before and after immersed in simulated pore solutions for 10 days were measured by Atomic force microscopy (AFM). AFM measurements were operated in tapping mode. The scanning area of AFM measurement was 3 μm×3 μm.

3. RESULTS AND DISCUSSION

3.1 EIS of steel bars in simulated pore solution

The EIS results of AR and NR immerse in the simulated PC, PSS and PSH pore solutions over 10 days are plotted in Figs.1-3, respectively.

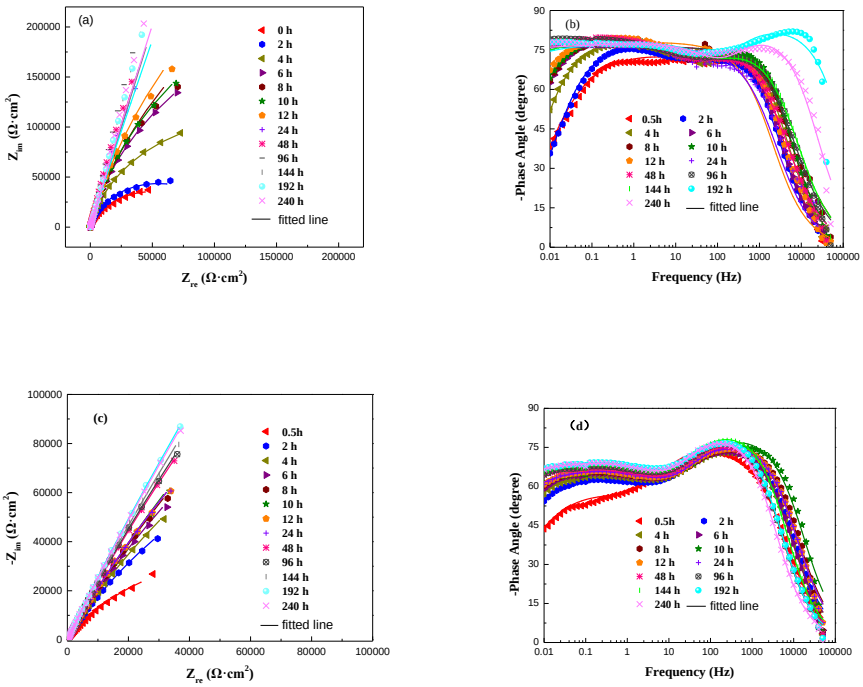

Fig.1 EIS plots of different steel bars immersing in PC simulated pore solution at different time.(a) Nyquist plots of NR, (b) Phase angle of Bode plots for NR, (c) Nyquist plots of AR, (d) Phase angle of Bode plots for AR

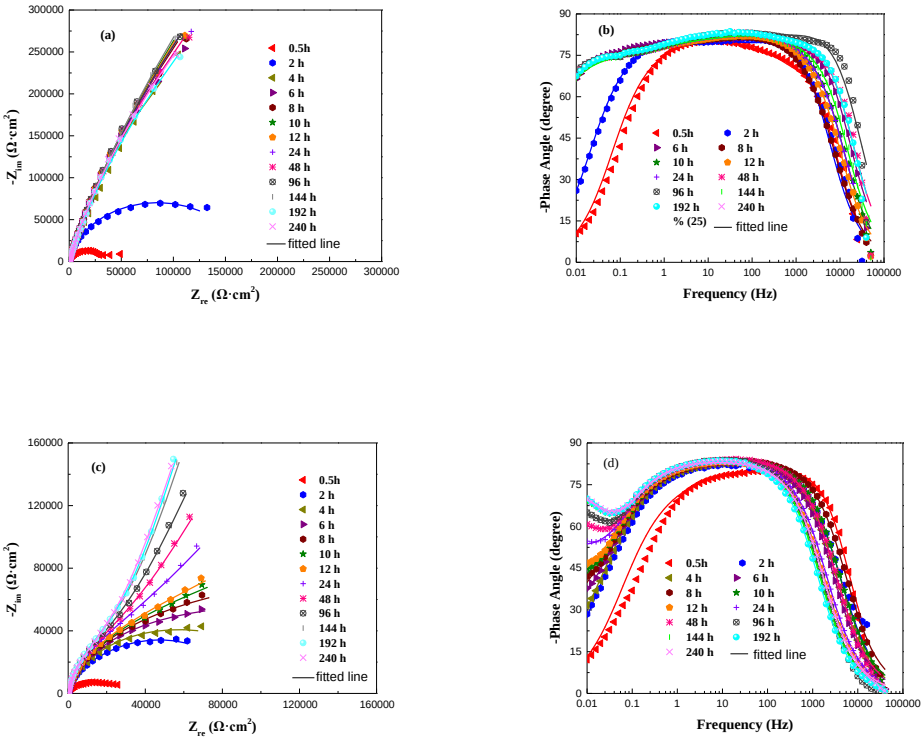

Fig.2 EIS plots of different steel bars immersing in PSH simulated pore solution at different time. (a) Nyquist plots of NR, (b) Phase angle of Bode plots for NR, (c) Nyquist plots of AR, (d) Phase angle of Bode plots for AR

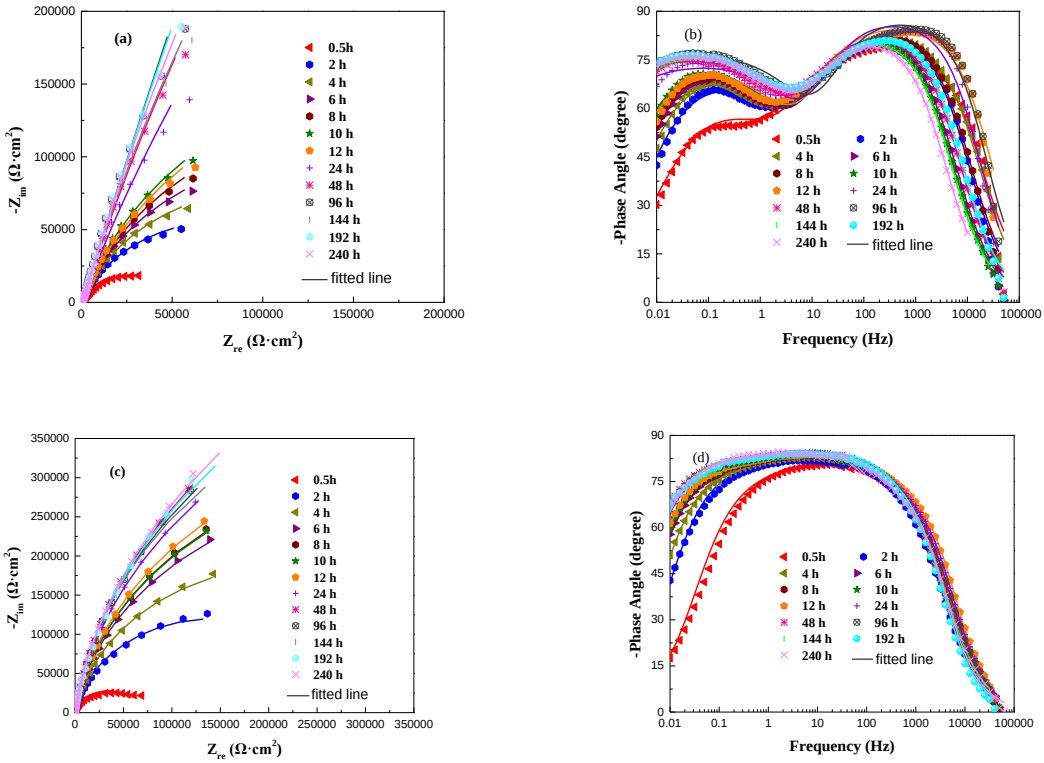

Fig.3 EIS plots of different steel bars immersing in PSS simulated pore solution for different time. (a) Nyquist plots of NR, (b) Phase angle of Bode plots for NR, (c) Nyquist plots of AR, (d) Phase angle of Bode plots for AR

It is generally believed that the capacitive arc in low frequency region of Nyquist plot is controlled by the charge transfer process, providing the information on charge transfer resistance and double-layer capacitance of the reinforcing bars [35]. The radius of the capacitive arc represents the size of the charge transfer resistance. While in high frequency region, the capacitive arc is derived from the feedback of resistance and capacitance of the passive film, and the radius of the capacitive arc is related to the resistance of passive film. From Figs. 1-3, it can be seen that the

capacitive arc of steel bar soaked in simulated pore solution of PC, PSH and PSS gradually increased with time, indicating that the steel bar was gradually passivated with time. For NR, it could be obviously seen that the impedance of the system in PSH simulated pore solution was higher than the other two samples in PC and PSS solution, which was higher than $2.5\times10^5\Omega\bullet cm^2$ after 240 h immersion. While for AR, the impedance of the system in PSS simulated pore solution was the highest, PSH followed next, and PC was the worst, which was less than $1.0\times10^5\Omega\bullet cm^2$ after 240h immersion.

As mentioned above, two time constants are present which represent the electrochemical responses of passive film and double layer, respectively. Thus, the equivalent circuit with two time constants as shown in Fig.4 was used to model the EIS data and the fitted values of each element can be used to describe the electrochemical reaction mechanism quantitatively.

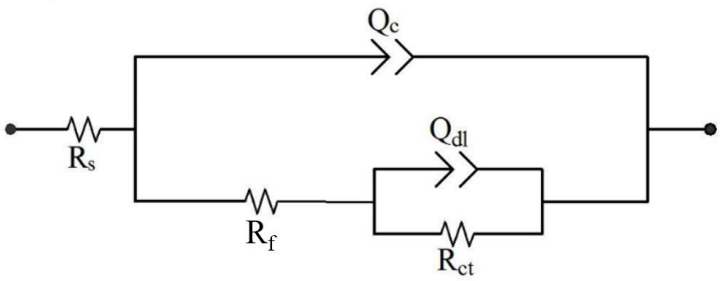

Fig.4 Equivalent circuit for steel bar/passive film system

Where, R_s is the solution resistance, R_f is resistance of the passive film, R_{ct} is the charge transfer resistance. Q_c represents the capacitance of the passive film and Q_{dl} represents the double layer capacitance of solution/steel bar. It should be noted that due to the porous and uneven surface of the passive film, the constant phase angle elements Q were usually used to replace the capacitance component [36].

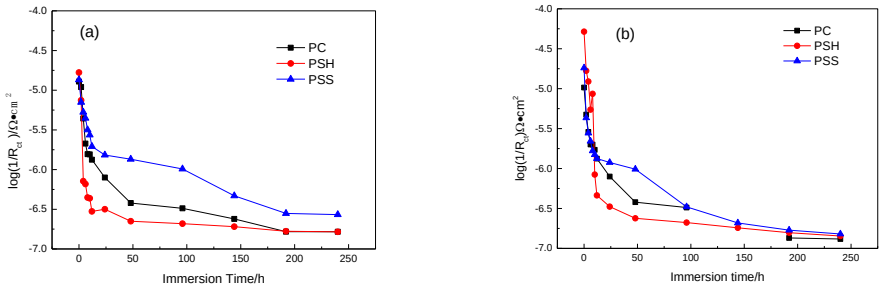

Fig.5 R_{ct} change rules of NR and AR in different simulated pore solution, (a) NR, (b) AR

The EIS plots were fitted. All the data are presented in Tables 3-8. And the R_{ct} results are present in Fig. 5. It can be seen that R_{ct} of NR and AR in PC, PSH and PSS increased rapidly during the first hour and then stabilized, which indicated that passive film started to grow as soon as bare steel was immersed in pore solutions and finally formed a stable passive film. The passive film played a protective role for the base metal and prevented the process of charge transfer. For NR, the growth period of passive film in PC, PSH and PSS were about 48h, 4h and 192h, individually. While for AR, the growth period of passive film in PC, PSH and PSS was about 48h, 12h and 96h, respectively. It can be concluded that in PSH, no matter what kind of matrix, the time limit of passive film stop growing is the shortest, while, in PSS, it is the longest. Therefore, the passivation process was closely related to the pH and the ion type of solution.

Table 3 Electrochemical impedance parameters for AR immersing in PC solution

		Q_c			Q_{dl}		
	R_s (Ω)	Y_{oc} ($S^n\Omega^{-1}\cdot cm^{-2}$)	n_c	R_f ($\Omega\cdot cm^2$)	Y_{odl} ($S^n\Omega^{-1}\cdot cm^{-2}$)	n_{dl}	R_{ct} ($\Omega\cdot cm^2$)
0.5 h	1.91	6.30E-05	0.85	619.00	1.06E-04	0.61	9.68E+04
2 h	1.42	4.40E-05	0.88	716.10	9.30E-05	0.66	2.11E+05
4 h	1.63	4.13E-05	0.88	654.10	8.40E-05	0.67	3.48E+05
6 h	1.63	3.96E-05	0.88	659.00	7.91E-05	0.68	5.00E+05
8 h	1.19	3.75E-05	0.89	621.80	7.71E-05	0.68	5.01E+05
10 h	2.87	3.15E-05	0.92	819.20	6.02E-05	0.71	5.83E+05
12 h	1.27	3.75E-05	0.89	678.70	7.40E-05	0.68	7.51E+05
24 h	1.27	3.75E-05	0.89	678.70	7.40E-05	0.68	1.26E+06
48 h	2.35	3.45E-05	0.90	854.90	6.56E-05	0.70	2.64E+06

96 h	2.27	3.31E-05	0.91	785.60	6.54E-05	0.70	3.08E+06
144 h	1.68	3.05E-05	0.92	731.10	6.47E-05	0.70	3.49E+06
196 h	2.19	3.25E-05	0.92	772.40	5.81E-05	0.71	7.40E+06
240 h	2.87	3.15E-05	0.92	819.20	6.02E-05	0.71	7.63E+06

Table 4 Electrochemical impedance parameters for NR immersing in PC solution

		Q_c			Q_{dl}		
	R_s (Ω)	Y_{oc} ($S^n\Omega^{-1}\cdot cm^{-2}$)	n_c	R_f ($\Omega\cdot cm^2$)	Y_{odl} ($S^n\Omega^{-1}\cdot cm^{-2}$)	n_{dl}	R_{ct} ($\Omega\cdot cm^2$)
0.5 h	2.42	3.19E-05	0.95	109.30	7.32E-05	0.74	7.79E+04
2 h	2.92	5.34E-05	0.89	459.00	3.14E-05	0.82	9.13E+04
4 h	2.05	4.35E-05	0.91	282.20	3.26E-05	0.83	2.27E+05
6 h	2.83	4.52E-05	0.90	407.10	2.49E-05	0.85	4.70E+05
8 h	1.84	4.41E-05	0.90	315.10	2.35E-05	0.84	6.39E+05
10 h	1.72	3.90E-05	0.92	317.70	2.85E-05	0.83	6.43E+05
12 h	2.67	4.76E-05	0.89	596.50	1.61E-05	0.87	7.51E+05
24 h	3.32	1.78E-05	1.00	232	6.26E-05	0.83	1.26E+06
48 h	2.31	1.80E-05	1.00	250	5.87E-05	0.82	2.64E+06
96 h	1.76	6.35E-05	1.00	437.8	6.36E-05	0.85	3.08E+06
144 h	1.89	3.53E-05	0.89	480	2.10E-05	0.82	4.18E+06
192 h	0.15	2.38E-05	0.94	163.2	3.12E-05	0.80	6.06E+06
240 h	0.65	2.34E-05	0.93	481.3	2.86E-05	0.80	6.07E+06

Table 5 Electrochemical impedance parameters for AR immersing in PSH solution

		Q_c			Q_{dl}		
	R_s (Ω)	Y_{oc} ($S^n\Omega^{-1}\cdot cm^{-2}$)	n_c	R_f ($\Omega\cdot cm^2$)	Y_{odl} ($S^n\Omega^{-1}\cdot cm^{-2}$)	n_{dl}	R_{ct} ($\Omega\cdot cm^2$)
0.5 h	0.79	3.31E-05	1.00	3.38E+01	6.99E-05	0.72	1.93E+04
2 h	1.47	6.01E-05	0.92	4.86E+01	1.11E-04	0.81	5.97E+04
4 h	1.76	5.49E-05	0.93	2.02E+01	2.01E-05	0.44	8.13E+04
6 h	2.21	1.49E-05	0.93	2.26E+00	1.60E-05	0.73	1.83E+05
8 h	1.50	2.75E-05	1.00	7.16E+01	3.25E-05	0.74	1.16E+05
10 h	1.57	4.97E-05	0.93	3.46E+01	2.74E-05	0.36	1.19E+06
12 h	3.28	5.09E-05	0.93	5.04E+04	3.56E-05	0.44	2.17E+06
24 h	3.07	4.72E-05	0.93	6.88E+04	4.52E-05	0.61	3.00E+06
48 h	2.00	4.42E-05	0.94	7.46E+04	4.48E-05	0.71	4.20E+06
96 h	4.33	4.23E-05	0.94	7.87E+04	4.16E-05	0.75	4.75E+06
144 h	4.87	4.09E-05	0.94	9.58E+04	3.88E-05	0.82	5.53E+06
192 h	5.42	4.08E-05	0.93	9.56E+04	3.85E-05	0.83	6.36E+06
240 h	4.12	4.29E-05	0.93	8.75E+04	3.75E-05	0.81	7.00E+06

Table 6 Electrochemical impedance parameters for NR immersing in PSH solution

		Q_c			Q_{dl}		
	R_s (Ω)	Y_{oc} ($S^n\Omega^{-1}\cdot cm^{-2}$)	n_c	R_f ($\Omega\cdot cm^2$)	Y_{odl} ($S^n\Omega^{-1}\cdot cm^{-2}$)	n_{dl}	R_{ct} ($\Omega\cdot cm^2$)
0.5 h	1.24	1.84E-05	1.00	2.08E+01	4.19E-05	0.82	5.98E+04
2 h	1.86	2.20E-05	0.96	3.54E+02	1.49E-05	0.79	1.34E+05
4 h	1.70	1.80E-05	1.00	7.06E+01	2.76E-05	0.83	1.40E+06
6 h	0.74	1.34E-05	1.00	3.16E+01	2.43E-05	0.79	1.52E+06
8 h	1.94	1.19E-05	1.00	1.89E+01	2.35E-05	0.78	2.25E+06
10 h	1.21	1.20E-05	1.00	2.20E+01	2.33E-05	0.78	2.30E+06
12 h	1.47	1.19E-05	1.00	2.08E+01	2.32E-05	0.77	3.36E+06
24 h	1.24	1.28E-05	0.99	2.25E+01	2.14E-05	0.76	3.16E+06
48 h	1.39	1.19E-05	1.00	2.00E+01	2.22E-05	0.77	4.47E+06
96 h	0.69	1.23E-05	1.00	3.01E+01	2.17E-05	0.77	4.80E+06
144 h	0.43	1.31E-05	1.00	4.86E+01	2.16E-05	0.76	5.24E+06
192 h	0.96	1.26E-05	1.00	2.38E+01	2.40E-05	0.77	5.99E+06
240 h	0.60	1.42E-05	1.00	3.57E+01	2.29E-05	0.77	6.08E+06

Table 7 Electrochemical impedance parameters for AR immersing in PSS solution

		Q_c			Q_{dl}		
	R_s (Ω)	Y_{oc} ($S^n\Omega^{-1}\cdot cm^{-2}$)	n_c	R_f ($\Omega\cdot cm^2$)	Y_{odl} ($S^n\Omega^{-1}\cdot cm^{-2}$)	n_{dl}	R_{ct} ($\Omega\cdot cm^2$)
0.5 h	2.36	1.95E-05	0.99	15.78	3.84E-05	0.81	5.50E+04
2 h	3.03	2.40E-05	0.96	28.39	2.15E-05	0.83	2.32E+05
4 h	2.35	1.92E-05	0.98	26.36	2.29E-05	0.84	3.60E+05
6 h	2.43	1.79E-05	0.99	28.56	2.20E-05	0.84	4.55E+05
8 h	2.76	1.69E-05	0.99	26.41	2.23E-05	0.85	6.01E+05
10 h	2.94	1.72E-05	0.99	24.51	2.23E-05	0.85	6.69E+05
12 h	1.99	1.71E-05	0.99	27.59	2.18E-05	0.85	7.50E+05
24 h	2.18	1.69E-05	0.99	25.71	2.12E-05	0.85	8.40E+05
48 h	2.52	1.72E-05	0.99	25.67	2.02E-05	0.86	1.02E+06
96 h	2.42	1.99E-05	0.97	26.89	1.78E-05	0.87	3.02E+06
144 h	2.69	3.32E-05	0.93	106.40	4.50E-06	0.95	4.80E+06
192 h	3.02	1.66E-05	1.00	37.25	1.72E-05	0.85	5.91E+06
240 h	3.39	1.34E-05	1.00	33.16	1.87E-05	0.86	6.60E+06

Table 8 Electrochemical impedance parameters for NR immersing in PSS solution

		Q_c			Q_{dl}		
	R_s (Ω)	Y_{oc} ($S^n\Omega^{-1}\cdot cm^{-2}$)	n_c	R_f ($\Omega\cdot cm^2$)	Y_{odl} ($S^n\Omega^{-1}\cdot cm^{-2}$)	n_{dl}	R_{ct} ($\Omega\cdot cm^2$)
0.5 h	0.61	4.20E-05	0.90	1.96E+03	1.01E-04	0.68	7.39E+04
2 h	1.12	2.67E-05	0.94	1.52E+03	7.05E-05	0.75	1.42E+05
4 h	0.78	2.84E-05	0.93	1.88E+03	6.36E-05	0.78	1.89E+05
6 h	2.03	2.71E-05	0.93	1.86E+03	6.12E-05	0.79	2.25E+05
8 h	1.09	2.55E-05	0.94	1.78E+03	5.91E-05	0.79	3.16E+05
10 h	2.35	2.67E-05	0.93	2.04E+03	5.46E-05	0.80	3.66E+05
12 h	0.43	2.18E-05	0.96	1.50E+03	5.92E-05	0.78	5.11E+05
24 h	0.70	1.72E-05	0.98	1.28E+03	4.99E-05	0.78	6.56E+05
48 h	1.99	2.14E-05	0.94	2.36E+03	3.77E-05	0.81	7.40E+05
96 h	0.57	1.48E-05	0.98	1.01E+03	4.10E-05	0.81	9.82E+05
144 h	2.91	2.17E-05	0.93	2.17E+03	3.44E-05	0.81	2.14E+06
192 h	1.84	1.97E-05	0.94	1.81E+03	3.50E-05	0.81	3.57E+06
240 h	3.82	2.18E-05	0.93	2.20E+03	3.40E-05	0.82	3.69E+06

3.2 Chemical composites and thickness of passive film

The XPS full spectra at the surface region of steel bars immersed in simulated pore solution of PC, PSH and PSS for 10 days are presented in Fig.6. Considering the thickness of passive film, the sputtering depths were 0, 6 nm, 12 nm, 18 nm and 24 nm.

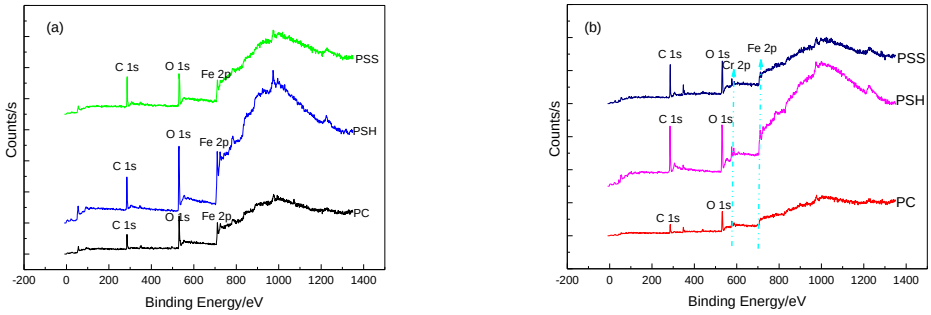

Fig.6 XPS spectrum of NR(a) and AR(b) with the sputtering depth of 0nm after 10 days immersion

From Fig.6, it can be seen that the elements of Fe and O mainly existed in NR, while Fe, O and Cr are present in the XPS spectrum of AR. This indicates that the composition of the passive film formed on the steel surface is significantly dependent on the composition of the steel.

Based on the deconvolution of the XPS spectra detected at various depths, the Fe2p、Cr2p spectrum at different sputtering depth of NR and AR immersing in alkali-activated slag simulated pore solution for 10 days were further analysed, and the results are presented in Figs.7-9. The area of each component at the depth of 0nm calculated by convolution were listed in Table 9.

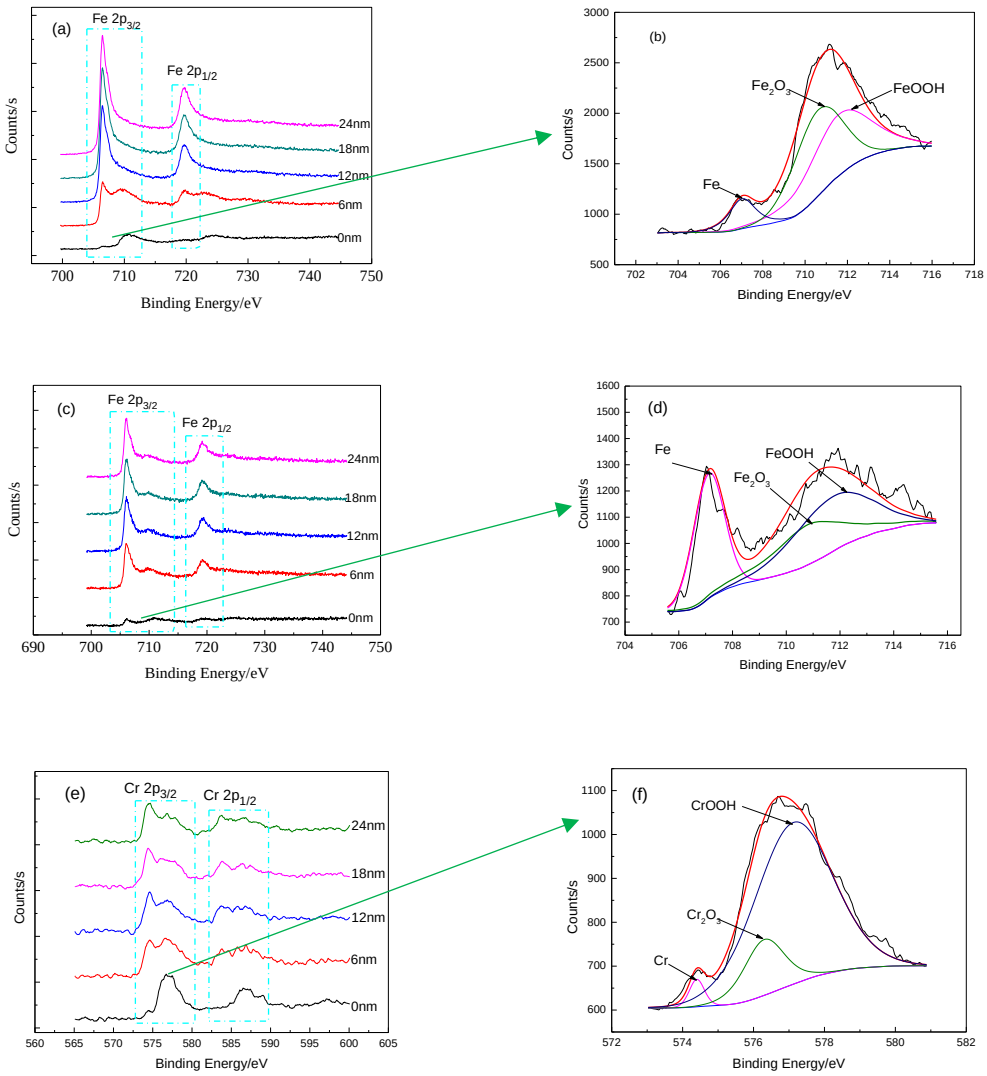

Fig.7 Fe2p、Cr2p spectrum of passive film with different sputtering depth for NR and AR steel immersing in PC solution for 10 days. (a) Fe 2p for NR, (c)Fe 2p for AR, (e)Cr 2p for AR, and

enlarged spectrum with 0nm sputtering depth of (d)Fe $2p_{3/2}$ for NR , (e)Fe $2p_{3/2}$ for AR , and (f) Cr $2p_{3/2}$ for AR.

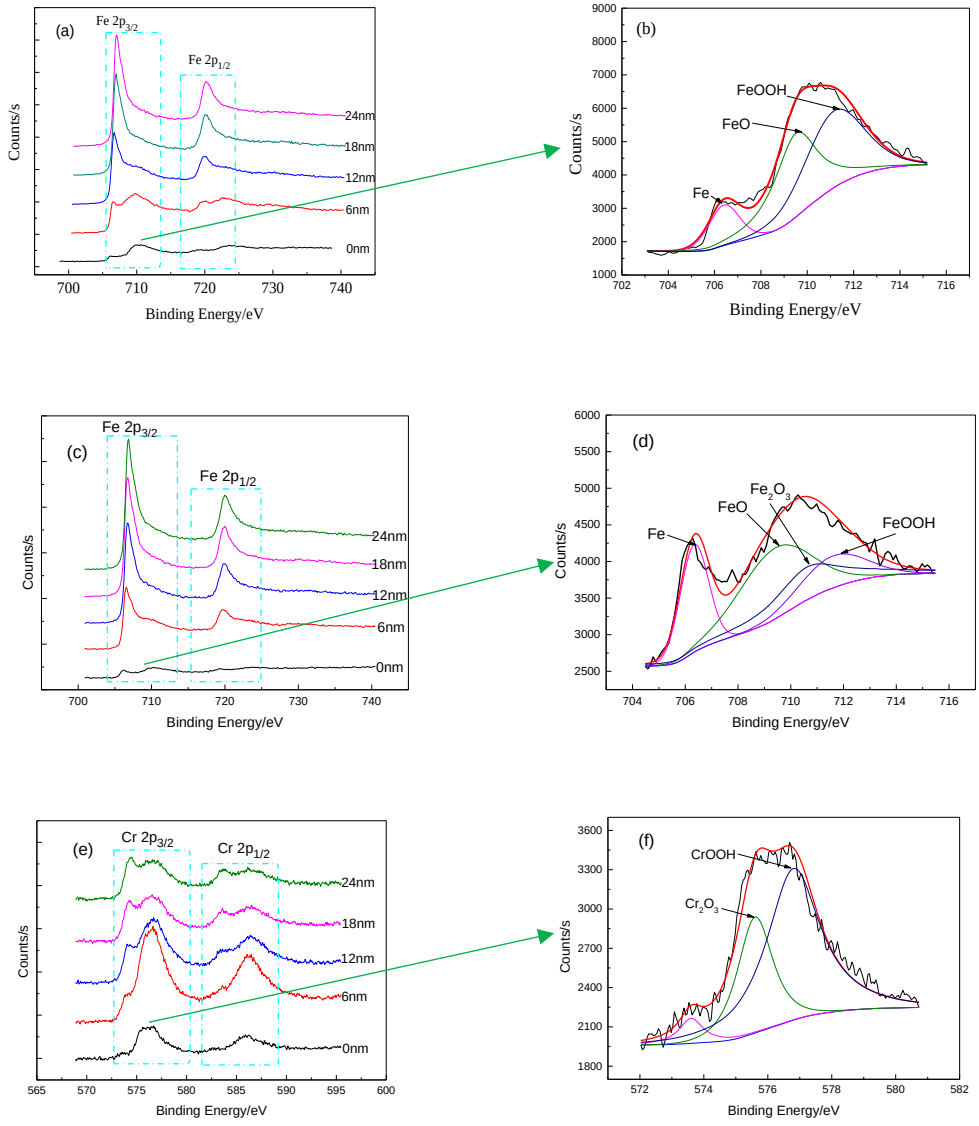

Fig.8 Fe2p、Cr2p spectrum of passive film with different sputtering depth for NR and AR steel immersing in PSH solution for 10 days, (a) Fe 2p for NR, (c)Fe 2p for AR, (e)Cr 2p for AR, and enlarged spectrum with 0nm sputtering depth of (d)Fe $2p_{3/2}$ for NR, (e)Fe $2p_{3/2}$ for AR, and (f) Cr $2p_{3/2}$ for AR.

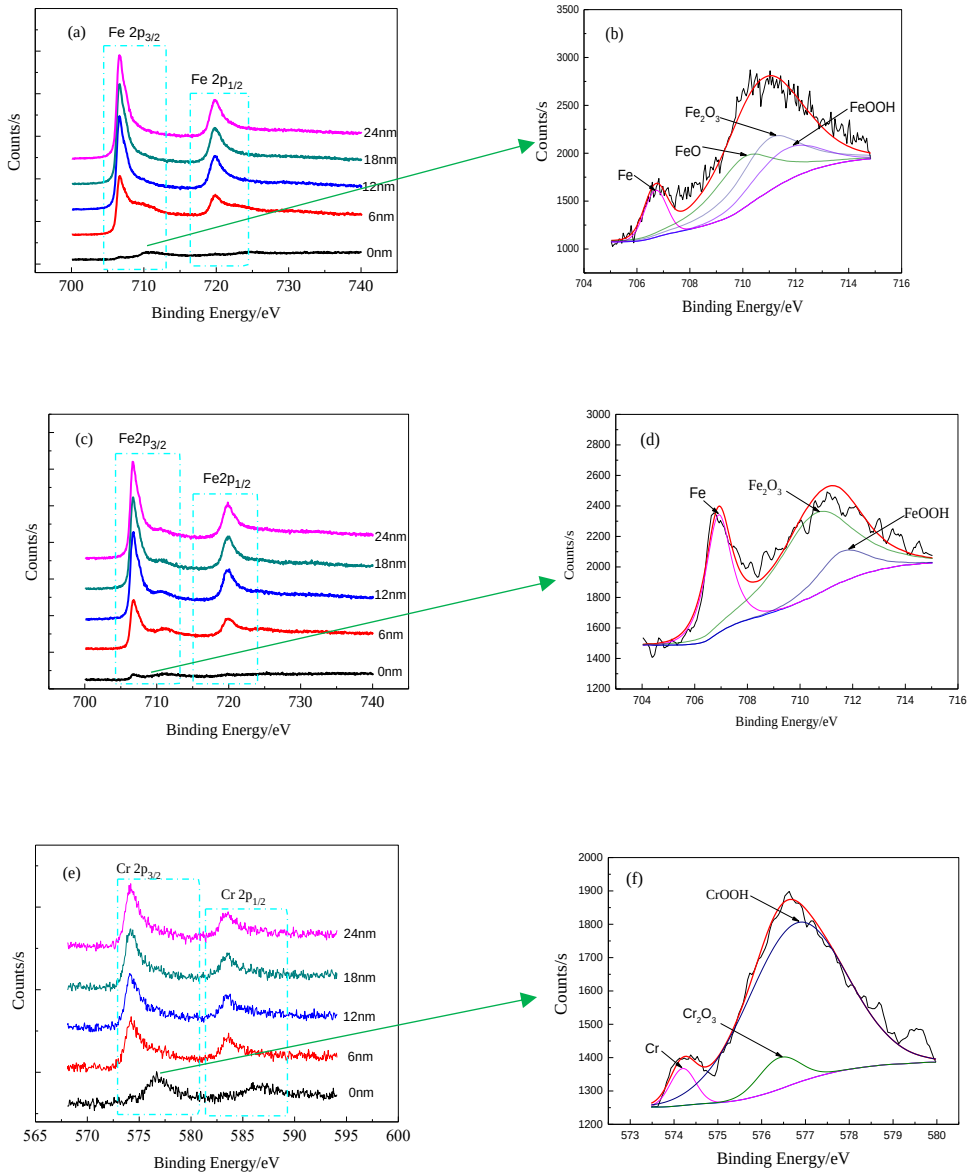

Fig.9 Fe2p、Cr2p spectrum of passive film with different sputtering depth for NR and AR steel immersing in PSS solution for 10 days, (a) Fe 2p for NR, (c)Fe 2p for AR, (e)Cr 2p for AR, and enlarged spectrum with 0nm sputtering depth of (d)Fe $2p_{3/2}$ for NR, (e)Fe $2p_{3/2}$ for AR, and (f) Cr $2p_{3/2}$ for AR.

Table 9 Area of passive film component at the depth of 0nm for NR and AR in different solutions.

solution	element	component	area	name in molecular dynamics model
PC	NR-Fe2p$_{3/2}$	FeOOH	2386	M1
		Fe_2O_3	2481	
	AR-Fe2p$_{3/2}$	FeOOH	789	M4
		Fe_2O_3	562	
	AR-Cr2p$_{3/2}$	Cr_2O_3	190	/
		CrOOH	1035	
PSH	NR-Fe 2p$_{3/2}$	FeOOH	7658	M2
		FeO	6793	
	AR-Fe2p$_{3/2}$	FeOOH	1367	M5
		FeO	3345	
		Fe_2O_3	2059	
	AR-Cr2p$_{3/2}$	CrOOH	3004	/
		Cr_2O_3	1365	
PSS	NR-Fe2p$_{3/2}$	FeOOH	1085	M3
		Fe_2O_3	1870	
		FeO	1740	
	AR-Fe2p$_{3/2}$	FeOOH	504	M6
		Fe_2O_3	2108	
	AR-Cr2p$_{3/2}$	CrOOH	1355	/
		Cr_2O_3	110	

From Figs.7-9 it can be seen that for NR samples, the passive film contained iron oxides, while for AR samples, the passivation film contained not only iron oxides, but also chromium oxides. And different split peaks could be observed at different binding energy. From Fig.7 it can be seen that, for NR and AR samples in PC, 710.6 eV and 711.6 eV were found to be Fe^{3+} (Fe_2O_3/FeOOH), the remaining one corresponded to Fe. Moreover, in the Cr 2p$_{3/2}$ spectrum in Fig. 7, the three peaks at binding energy of 574.4 eV, 581.0 eV and 576.5 eV corresponded to the Cr, CrO_3 and Cr_2O_3, respectively. As comparison, for NR and AR samples in PSH, the binding energy of Fe 2p$_{3/2}$ at 706.4 eV, 709.5 eV, 710.6 eV and 711.6 eV were assigned to Fe, FeO, Fe_2O_3 and FeOOH, respectively, as shown in Fig.8. In addition, the peak at 573.6 eV, 577.9 eV 576.0 eV was assigned to Cr, CrO_3 and Cr_2O_3, respectively. For NR and AR samples in PSS, as shown in Fig. 9, the binding

energy of Fe $2p_{3/2}$ at 706.7 eV, 710.0 eV, 711.0 eV, 711.6 eV corresponded to Fe, FeO, Fe_2O_3 and FeOOH, respectively. Additionally, the combination energy of Cr $2p_{3/2}$ were 574.1 eV, 579.4 eV and 576.7 eV, corresponding to the Cr, CrO_3 and Cr_2O_3, respectively. In addition, with the increase of sputtering depth, the peak width decreased, the content of Fe increased, and the content of iron oxides reduced. For AR, the content of Cr increased but the chromium oxides reduced.

Fe element in the passive film originated from the outward diffusion of steel matrix, which resulted in the gradual variation of Fe content through the passive film. The content of iron oxide decreased with the sputtering depth while the content of iron increased with the sputtering depth throughout the passive film. Thus, the changing law of ratio of Fe oxide to Fe (RFF) could be employed to evaluate the thickness of passive film [37]. The lower RFF value indicated the thinner of the passive film. And the RFF value of NR and AR steel bar immersing in different solutions with sputtering depth are presented in Fig.10.

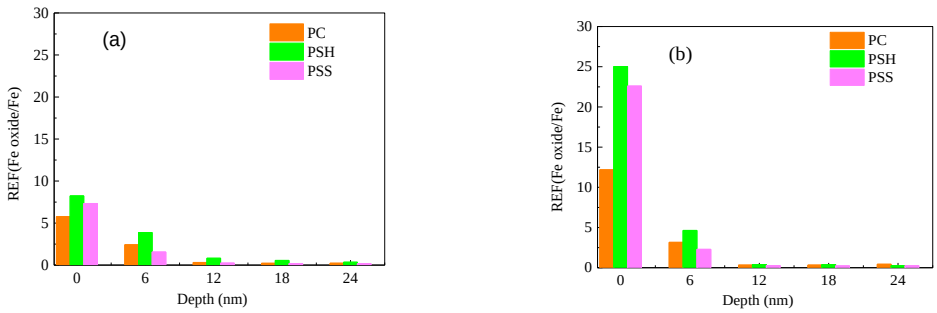

Fig.10 RFF of NR and AR steel bar immersing in different solutions with sputtering depth (a)NR steel bar (b) AR steel bar

Obviously, the RFF decreased with sputtering depth whether for NR or AR. For NR steel bars soaped in PC, the surface RFF was 5.759, while at 12 nm depth, it decreased to be 0.317, and then, kept stable. So, it can be speculated that the passive film could be regarded as 12 nm according to the changing tendency. By the same way, the thickness of passive film of NR steel bars in PSH and PSS were about 18 nm and 12 nm, individually. For AR steel bars immersed in three kinds of the simulated solutions, the thickness of the passive film was basically the same, which was about 12 nm.

3.3 Microstructure of passive film of steel bar

The AFM morphology for NR and AR steel bars are presented in Fig.11. All of the steel bars were ground and polished in the same manner, resulting in the presence of stripes on the surface as displayed in Fig. 11(a) and (b). Moreover, the height differences of the surface were about 60 nm and 110 nm for bare NR and AR, respectively. On the other hand, for NR with 3×3 μm^2 scanning area, the average roughness (R_a) and root-mean-square roughness (R_q) were 6.09 nm and 7.79 nm, respectively. For AR with 3×3 μm^2 scanning area, R_a and R_q were found to be 10.5 nm and 14.3 nm, respectively. The AFM morphology of steel bars immersing in PC, PSH and PSS for 10 days are showed in Fig.11 (c)-(h). When steel bars are passivated in PC simulated pore solution, the original grinding stripes still exist on the surface of steel bars, but some columnar particles can be seen in the deep grooves of the stripes, and the size of the particles generated on the surface of AR steel bars was much larger. In comparison, the passive films formed in PSH and PSS solutions were more compact, which cover the surface of NR and AR and thereby the grinding stripes on the surface of NR and AR were hidden.

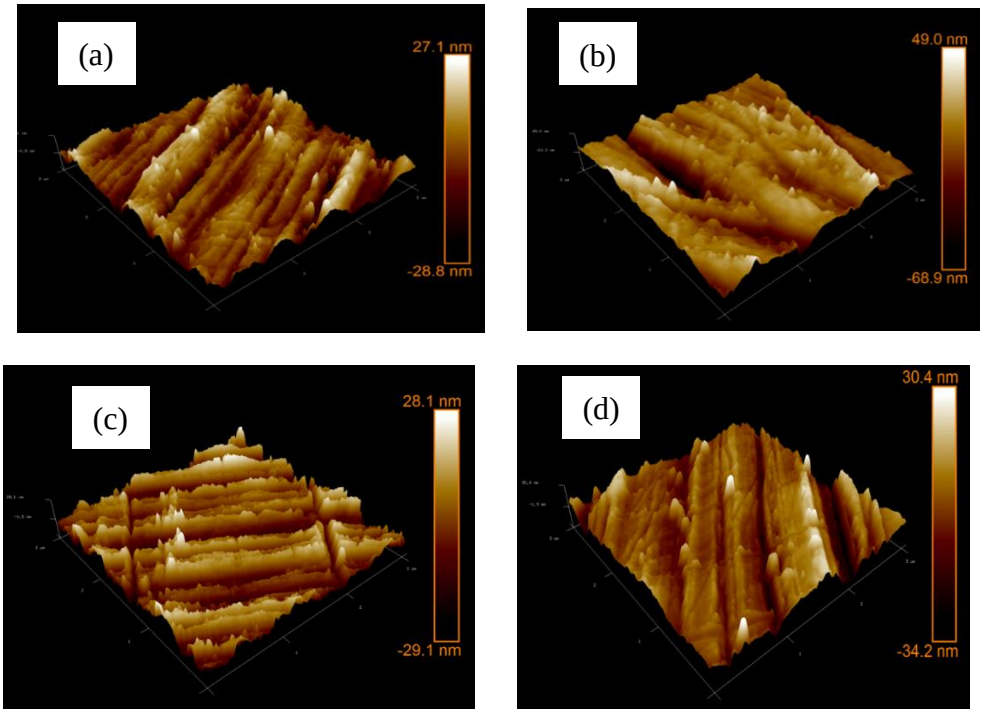

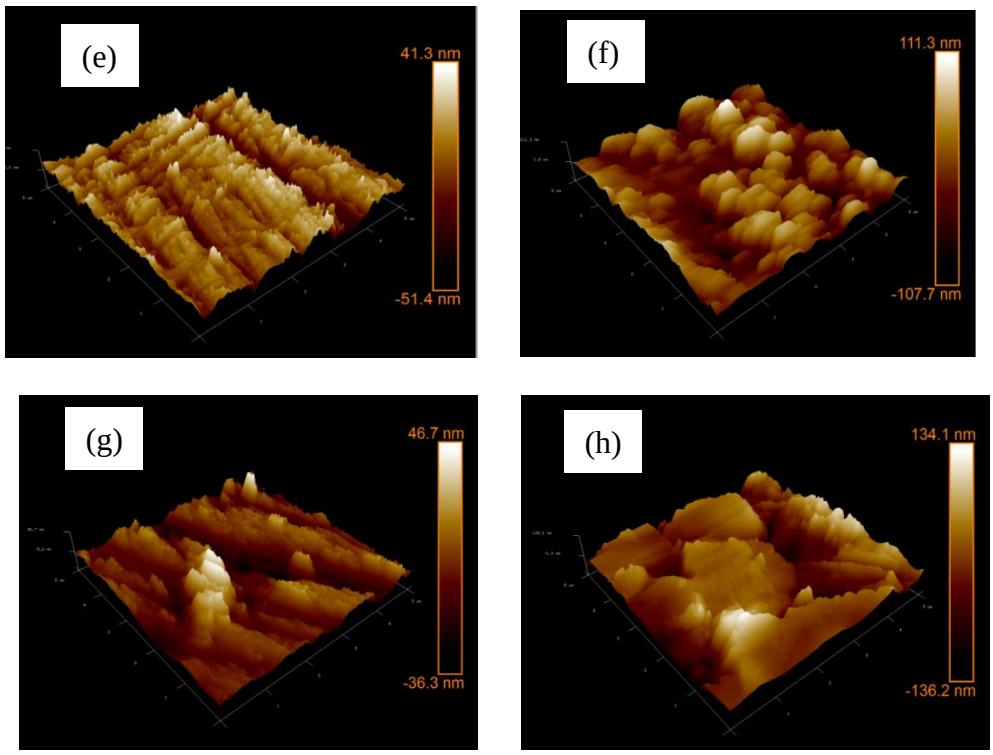

Fig.11 AFM morphology of NR and AR steel bar without passive film, (a) pure NR, (b) pure AR; AFM morphology of NR and AR steel bar immersing in different solutions for 10 days, (c) NR in PC, (d)AR in PC, (e) NR in PSH, (f) AR in PSH, (g) NR in PSS, (h) AR in PSS

3.4 Molecular Dynamics

Based on the theory of molecular dynamics, the interface properties between the passive film and the matrix Fe were studied. The surface structure model of iron adsorbed by steel passive film in aqueous solution was established. The interaction energy of different component with Fe atoms were characterized by mean square displacement (MSD) and the change of interface binding energy.

The compositions of passive film were divided into six types according to the XPS results in Table 9. Correspondingly, six initial models were established in Fig.12, which were individually named M1, M2, M3, M4, M5 and M6. Fe atom was selected as the model substrate. According to the composition proportion of passive film, Fe, FeOOH, FeO and Fe_2O_3 were arranged and adsorbed on the Fe substrate in proportion. The initial size of each model was 17.20 × 17.20 × 72.90 $Å^3$. The periodic boundary condition was used in the calculation process, which made the model extend

infinitely in space. In order to simulate the effect of water environment on the passive film, 539 water molecules with a density of 0.98 g/cm^3 were randomly added to the upper layer of Fe atom and passive film. A vacuum layer of 30 μm was also added above the model to counteract the interaction between the upper and lower interfaces.

The initial structure model was optimized by 500 picosecond to keep the energy difference within 100 kcal/mol. The force calculation module was used to conduct a 20 picosecond kinetic relaxation process for the four initial models, so that the water molecules can fully react with the passive film to achieve a stable structure. In the process of simulation, COMPASS force field was selected, NVT ensemble was used, the temperature was 298 K, the cut-off distance was 12.5 Å, and the time step was 1.00 femtosecond.

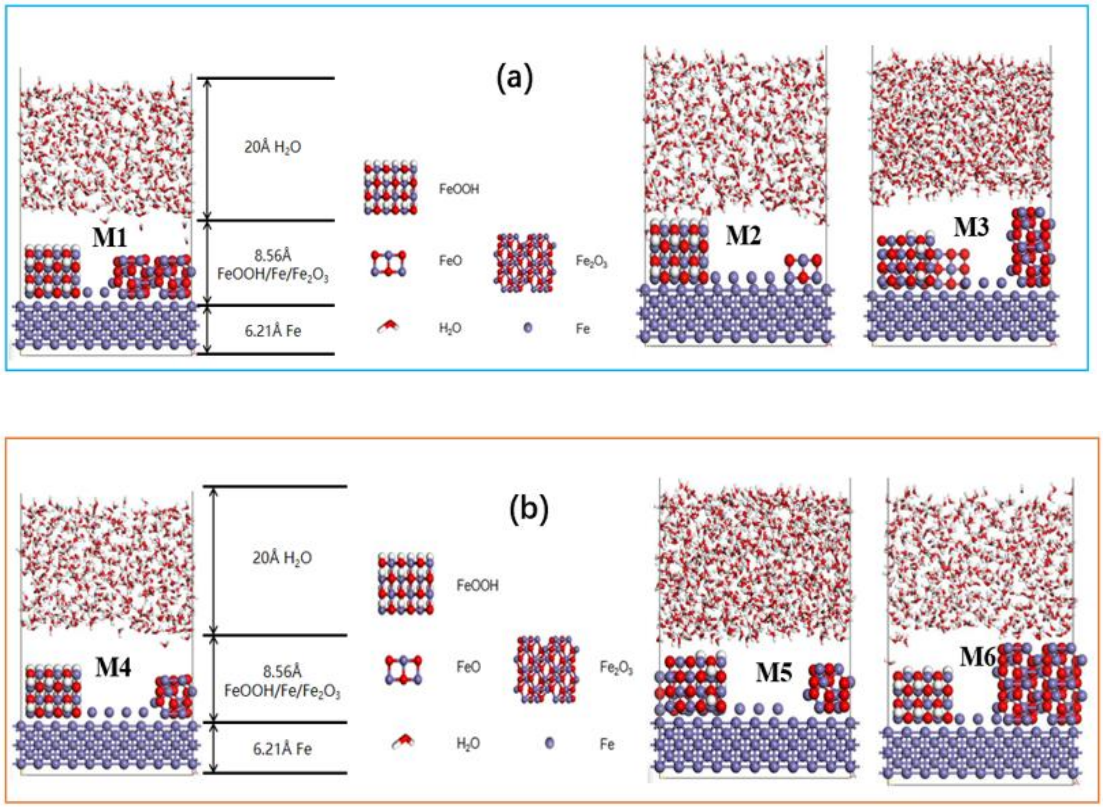

Fig.12 Basic model for initial simulation (a) M1, M2, and M3 for NR, (b) M4, M5, and M6 for AR

Fig.12 illustrated the initial calculation model of water permeation environment. Water molecules would invade the interface between the passive film and Fe atoms, resulting in the weakening of the interaction bonding effect, which could be evaluated by the interaction energy (E_i)

of passive film and water. The lower the E_i was, the stronger the binding force between water and Fe atom base would be, which could be obtained by formula (1):

$$E_i = E_t - E_1 - E_2 \quad (1)$$

Where, E_t was the total energy of the model, E_1 was the energy of passive film, E_2 was the energy of water layer.

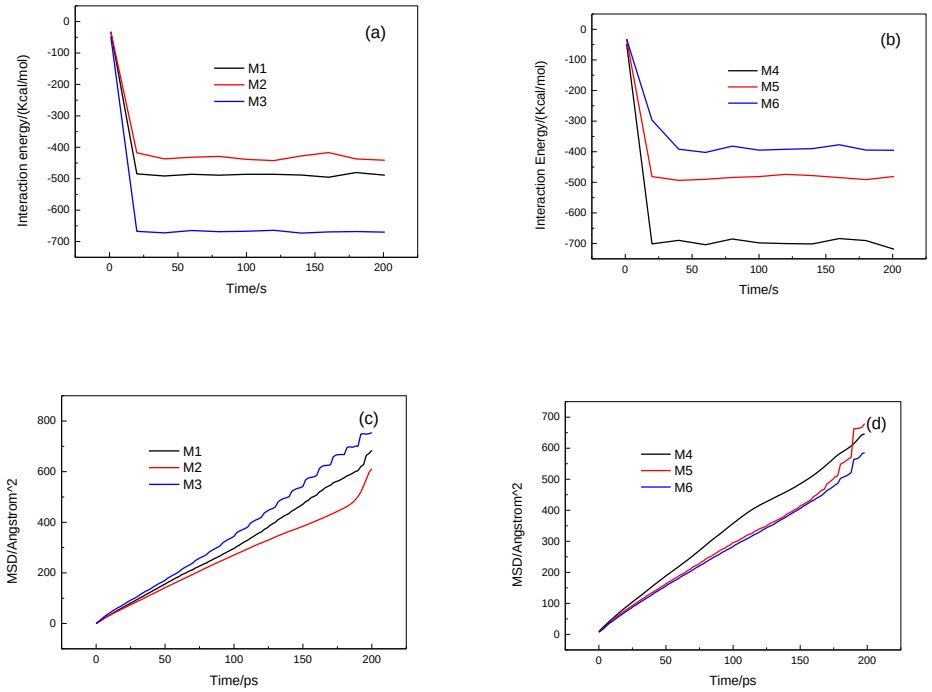

Fig.13 Change of interaction energy (a),(b) and MSD (c),(d) of different models with time

The mean square displacement (MSD) was an important parameter of dynamic analysis, which was the statistical mean of the particle trajectory changing with time. It can be used to evaluate the motion characteristics of water molecules or ions. The formula was as follows.

$$MSD = < \left| r_i(t) - r_i(0) \right|^2 > \quad (2)$$

Where, $r_i(t)$ represented the position of atom i at time t, and $r_i(0)$ represents the initial position of atom i. The larger the MSD over time, the faster the diffusion of water molecules. MSD of water molecule in six models was obtained after analyzing O atom's MSD by Forcite Analysis Module.

As shown in Fig.13 (a) and (b), the interaction energy between water and passive film was reduced with time while the binding force was improved with time. It can be seen that the binding force between water and passive film of M2 model in Fig.13 (a) and M6 model in Fig.13 (b)was the strongest.

As shown in Fig.13, the diffusion rate of water molecules had an obvious rule as follows, M3 > M1 > M2, M4>M5>M6. Different components of passive film affected the adsorption strength of water molecules, resulting in different diffusion rate of water molecules. The stronger the barrier ability of the passive film, the slower the diffusion rate of water molecules, and the smaller the MSD value. According to the interface interaction in Fig.13 (a) and (b), under the same conditions, the barrier ability of passive film followed the rule of M2 >M1 > M3 and M6>M5>M4.

In the simulated pore solution of alkali- activated system (PSS / PSH), the silicate ions on the surface of reinforcement or silica gel formed by alkali silicon reaction will form an adsorption layer with zeolite structure [38]. While, the passive film on the steel surface in the simulated cement pore solution presents a double layer structure [39], which is different from the composition and structure of the passive film formed by the alkali- activated system. Combined with table 1 in this study, the Fe content in alkali-activated simulated pore solution is higher than that in PC simulated pore solution. Therefore, the total content of Fe oxide in model M2 and M3 is higher than that in M1, and the content of Fe oxide in M5 and M6 is higher than that in M4.

For NR without chromium element, it can be seen from Figs.7-9 and Table 9 that FeO/FeOOH (M2) was the main component of passive film in PSH solution, $FeOOH/Fe_2O_3$ (M1) was the main component of passive film in PC solution, FeO/Fe_2O_3/FeOOH (M3) was the main component of passive film in PSS solution. Combined with Fig.11 it can be concluded that the protective performance of passive film in PSH was the strongest, because the diffusion rate of water molecules in it was the weakest, which meant that M2 could prevent water molecules from spreading to the base metal surface for better protection effectively. While for PC and PSS, the diffusion rate of water molecules was relative fast, which led to poor protection capability. And all the above results were consistent with that of EIS.

For AR with chromium element, it can be seen from Figs.7-9 and Table 9 that besides Cr_2O_3/CrOOH, $FeOOH/Fe_2O_3$ (M4) was the main component of passive film in PC solution,

$FeO/Fe_2O_3/FeOOH$ (M5) was the main component of passive film in PSH solution, $Fe_2O_3/FeOOH$ (M6) was the main component of passive film in PSS solution. Combined with Fig.11 it can be concluded that the protective performance of passive film in PSS was the strongest, because the diffusion rate of water molecules in it was the weakest, which meant that M6 could prevent water molecules from spreading to the base metal surface for better protection. While for PC and PSH, the diffusion rate of water molecules was faster, which led to smaller protection capability. These results were coincided with that of EIS.

4. Conclusions

The passivation of low-carbon steel bar and corrosion-resistant steel bar immersed in ordinary Portland cement concrete, NaOH, and waterglass activated GGBS simulated pore solution were investigated in current study via EIS methods, XPS and AFM By analysing the electrochemical behaviour and properties of passive film of steel bar, it became evident that the passive film would be formed in alkali active GGBS concrete, and its properties were influenced by activators. In brief, based on the experimental results and analysis as described in this paper, main conclusions can be drawn as follows:

(1) The corrosion current of reinforcing steel tends to be stable and passive film forms gradually when the steel bars were immersed in the simulated pore solution of alkali-activated slag. The formation time of passive film of NR steel bar in PC, PSH and PSS simulated pore solution were 48 h, 4 h and 192 h, separately. The formation time of passive film of AR steel bars in PC, PSH and PSS simulated pore solution were 48 h, 12 h and 96 h, individually.

(2) In alkali-activated slag simulated pore solution, the passive film of NR steel bar was mainly composed of Fe and O elements. The outer layer of passive film was composed of Fe^{2+} (FeO) and Fe^{3+} ($Fe_2O_3/FeOOH$). The passive film of AR steel bar was mainly composed of Fe, O and Cr. The outer layer of passive film was mainly composed of Fe^{2+}(FeO)、Fe^{3+}($Fe_2O_3/FeOOH$), Cr_2O_3 and CrOOH.

(3) According to the evolution rule of the ratio of Fe oxides/Fe elements on the surface of steel bars obtained by XPS technology, the thickness of passive film for NR steel bars were 12 nm, 18 nm and 12 nm in PC, PSH and PSS solutions, respectively. And the passive film thickness of AR

steel bar in the above three simulated pore solutions was all about 12 nm.

(4) The passive films formed in PSH and PSS were more compact, and a large number of plate-like and block structures were formed on the surface of AR steel bars. Comparing with NR steel bars, the passive film of corrosion resistant steel bars was more compact and stable.

(5) Molecular Dynamics results indicated that MSD and Ei could be used to characterize the protective ability of the passive film. The binding force between the passive film and Fe base was improved with time. Different composition of passive film would result in different diffusion rate of water molecule as well as different protective ability of the passive film. All the results obtained from molecular dynamics in the three solutions were in accordance with those of EIS.

(6) In this work, the results are mainly based on simulated pore solution without sulfur ions, but the actual AAM concrete pore solution contains various kinds of sulfur ions. Moreover, the service environment of steel bar is significantly different from that of simulated pore solution, which may have great influence on the formation and damage process of the passive film and will be a focus of future research.

Acknowledgements

This work is a part of a series of projects financially supported by the National Natural Science Foundation of China (NSFC), Grant No. U1806225 and 52078259, 5191102012, and the MOUNT TAI SHAN Scholar of Shandong Province (ts20190942). Besides, this work is also supported by National 111 project. All these supports are gratefully appreciated.

Data Availability

The raw/processed data required to reproduce these findings cannot be shared at this time as the data also forms part of an ongoing study.

References:

[1] E. Gartner, Industrially interesting approaches to 'low-CO_2' cements, Cement Concrete Res. 34 (2004) 1489-1498. https://doi.org/10.1016/j.cemconres.2004.01.021.

[2] J. Liu, G. Ou, Q. Qiu, X. Chen, J. Hong, F.Xing, Chloride transport and microstructure of concrete with/without fly ash under atmospheric chloride condition, Constr. Build. Mater.146 (2017) 493-501. https://doi.org/10.1016/j.conbuildmat.2017.04.018.

[3] H. Chen, S. Huang, C. Tang, Effect of curing environments on strength, porosity and chloride ingress resistance of blast furnace slag cement concretes: A construction site study, Constr. Build. Mater. 35 (2012) 1063-1070. https://doi.org/10.1016/j.conbuildmat.2012.06.052.

[4] S. Mahmoud Abdelkader, E. Reyes Pozo, A. Moragues Terrades, Evolution of microstructure and mechanical behavior of concretes utilized in marine environments, Mater. Design 31 (2010) 3412-3418. https://doi.org/10.1016/j.matdes.2010.01.045.

[5] Cement Part 1: Composition, specification and conformity criteria for common cements. BS EN 197-1:2011.

[6] M.A. Megat Johari, J.J. Brooks, S. Kabir, P. Rivard, Influence of supplementary cementitious materials on engineering properties of high strength concrete, Constr. Build. Mater. 25(5) (2011) 2639-2648. https://doi.org/10.1016/j.conbuildmat.2010.12.013.

[7] E. Güneyisi, M. Gesoğlu, A study on durability properties of high-performance concretes incorporating high replacement levels of slag, Mater. Struct. 41 (2008) 479-493. https://doi.org/10.1617/s11527-007-9260-y.

[8] P.H.R. Borges, J.O. Costa, N.B. Milestone, C.J. Lynsdale, R.E. Streatfield, Carbonation of CH and C–S–H in composite cement pastes containing high amounts of BFS, Cement Concrete Res. 40 (2010) 284-292. https://doi.org/10.1016/j.cemconres.2009.10.020.

[9] C. O. Nwankwo, G. O. Bamigboye, I. E.E. Davies, T. A. Michaels, High volume Portland cement replacement: A review, Constr. Build. Mater. 260 (2020) 120445. https://doi.org/10.1016/j.conbuildmat.2020.120445.

[10] H. Rostami, W. Brendley, Alkali ash material: A novel fly ash-based cement, Environ. Sci. Technol. 37(2003) 3454-3457. https://doi.org/10.1021/es026317b.

[11] D. M. Roy, W. Jiang, M.R. Silsbee, Chloride diffusion in ordinary, blended, and alkali-activated cement pastes and its relation to other properties, Cement Concrete Res. 30 (2000) 1879-1884. https://doi.org/10.1016/S0008-8846(00)00406-3.

[12] Y. Ding, J. Dai, C. Shi, Mechanical properties of alkali-activated concrete: A state-of-the-art review, Constr. Build. Mater. 127 (2016) 68-79. https://doi.org/10.1016/j.conbuildmat.2016.09.121.

[13] H. Zhu, Z. Zhang, Y. Zhu, L. Tian, Durability of alkali-activated fly ash concrete: Chloride penetration in pastes and mortars, Constr. Build. Mater. 65 (2014) 51-59. https://doi.org/10.1016/j.conbuildmat.2014.04.110.

[14] C. Shi, D. Roy, P. Krivenko, Alkali-Activated Cements and Concretes, CRC Press, Boca Raton, 2006.

[15]K. W. Shah, G. F. Huseien, Bond strength performance of ceramic, fly ash and GBFS ternary wastes combined alkali-activated mortars exposed to aggressive environments, Constr. Build. Mater. 251(2020)119088. https://doi.org/10.1016/j.conbuildmat.2020.119088.

[16]I. Amer, M. Kohail, M.S. ElFeky, A. R. Ibraheem, M. A. Khalaf, A review on alkali-activated slag concrete, Ain Shams Eng. J. 12 (2021) 1475-1499. https://doi.org/10.1016/j.asej.2020.12.003.

[17] Z. Jin, T. Zhao, B. Wang, H. Chang, Relative humidity response of concrete under marine environment, Journal of Central South University (Science and Technology) 45 (2015) 3608-3613.

[18] Z. Tang, W. Li, Y. Hu, J. L. Zhou, V. W.Y. Tam, Review on designs and properties of multifunctional alkali-activated materials (AAMs), Constr. Build. Mater. 200 (2019) 474-489. https://doi.org/10.1016/j.conbuildmat.2018.12.157.

[19] J. Osio-Norgaard, J. P. Gevaudan, W. V. I. Srubar, A review of chloride transport in alkali-activated cement paste, mortar, and concrete, Constr. Build. Mater. 186 (2018) 191-206. https://doi.org/10.1016/j.conbuildmat.2018.07.119.

[20] A. Adam, Strength and durability properties of alkali activated slag and fly ash-based geopolymer concrete. Doctor of Philosophy (PhD), (2009), RMIT University.

[21] W. A. Chaparro, J. H. B. Ruiz and R. d. J. T. Gómez, Corrosion of reinforcing bars embedded in alkali-activated slag concrete subjected to chloride attack, Mater. Res. 15 (2012) 57-62. https://doi.org/10.1590/S1516-14392011005000096.

[22] P. S. Mangat, Olalekan O. Ojedokun, Bound chloride ingress in alkali activated concrete, Constr. Build. Mater. 212 (2019) 375-387. https://doi.org/10.1016/j.conbuildmat.2019.03.302.

[23] F. Puertas, M. Torres-Carrasco, Use of glass waste as an activator in the preparation of alkali-activated slag. Mechanical strength and paste characterisation, Cement Concrete Res. 57 (2014) 95-104. https://doi.org/10.1016/j.cemconres.2013.12.005.

[24] C. Monticelli, M.E. Natali, A. Balbo, Corrosion behavior of steel in alkali-activated fly ash mortars in the light of their microstructural, mechanical and chemical characterization, Cement Concrete Res. 80 (2016) 60-68. https://doi.org/10.1016/j.cemconres.2015.11.001.

[25] J.M. Miranda, A. Ferna´ndez-Jime´nez, J.A. Gonza´lez, Corrosion resistance in activated fly ash mortars, Cement Concrete Res. 35 (2005) 1210-1217. https://doi.org/10.1016/j.cemconres.2004.07.030.

[26] M. Criado, S. Martínez-Ramirez, J.M. Bastidas, A Raman spectroscopy study of steel corrosion products in activated fly ash mortar containing chlorides, Constr. Build. Mater. 96 (2015) 383-390. https://doi.org/10.1016/j.conbuildmat.2015.08.034.

[27] Z. Ai, J. Jiang, W. Sun, X.Jiang, B.Yu, K. Wang, Z.Zhang, Enhanced passivation of alloy corrosion-resistant steel Cr10Mol under carbonation - Passive film formation, the kinetics and mechanism analysis, Cement Concrete Comp. 2018 (92) 178-187. https://doi.org/10.1016/j.cemconcomp.2018.06.005.

[28] I. G. Ogunsanya, C.M. Hansson, The semiconductor properties of passive films and corrosion behavior of stainless-steel reinforcing bars in simulated concrete pore solution, Materialia 6 (2019) 100321. https://doi.org/10.1016/j.mtla.2019.100321.

[29] M. Criado, D.M. Bastidas, S. Fajardo, Corrosion behaviour of a new low-nickel stainless steel embedded in activated fly ash mortars, Cement Concrete Comp. 33 (2011) 644–652. https://doi.org/10.1016/j.cemconcomp.2011.03.014.

[30] X. Yu, L. Jiang, J. Xu, Y. Zu, Effect of Na_2SiO_3 content on passivation and corrosion behaviour of steel in a simulated pore solution of Na_2SiO_3-activated slag, Constr. Build. Mater.146 (2017) 156-164. https://doi.org/10.1016/j.conbuildmat.2017.04.091.

[31] A. Gruskovnjak, B. Lothenbach, L. Holzer, R. Figi, F. Winnefeld, Hydration of alkali-activated slag: comparison with ordinary Portland cement, Adv. Cem. Res. 18 (2006) 119-128. https://doi.org/10.1680/adcr.2006.18.3.119.

[32] U. Angst, B. Elsener, C. K. Larsen, Øystein Vennesland, Critical chloride content in reinforced concrete - A review, Cement Concrete Res. 39 (2009) 1122-1138. https://doi.org/10.1016/j.cemconres.2009.08.006.

[33] W. Wang, H. Chen, X. Li, Z. Zhu, Corrosion behavior of steel bars immersed in simulated pore solutions of alkali-activated slag mortar, Constr. Build. Mater. 143 (2017) 289-297. https://doi.org/10.1016/j.conbuildmat.2017.03.132.

[34] G. Geng, J. Shi, W. Sun, Comparison of stationary and transient electrochemical measurements for steel corrosion in simulated concrete pore solution, Corrosion science and protection technology 23 (2011) 323-329.

[35] J. Ress, U. Martin, J. Bosch, D.M. Bastidas, pH-Triggered Release of $NaNO_2$ Corrosion Inhibitors from Novel Colophony Microcapsules in Simulated Concrete Pore Solution, ACS Appl. Mater. Inter. 129 (2020) 46686−46700. https://doi.org/10.1021/acsami.0c13497.

[36] G. Tranchida, F.Di Franco, B. Megna, M. Santamaria, Semiconducting properties of passive films and corrosion layers on weathering steel, Electrochim. Acta 354 (2020) 136697. https://doi.org/10.1016/j.electacta.2020.136697.

[37] Z. J. Zheng, Y. Gao, Y. Gui, M. Zhu, Studying the fine microstructure of the passive film on nanocrystalline 304 stainless steel by EIS, XPS, and AFM, J. Solid State Electr. 18 (2014) 2201–2210. https://doi.org/10.1007/s10008-014-2472-5.

[38] J. Shi, J. Ming, W. Sun, Electrochemical behaviour of a novel alloy steel in alkali-activated slag mortars, Cement Concrete Comp. 92 (2018)110-124.
https://doi.org/10.1016/j.cemconcomp.2018.06.004.

[39] M. Sánchez, J. Gregori, C. Alonso, J.J. García-Jareño, H. Takenouti, F. Vicente, Electrochemical impedance spectroscopy for studying passive layers on steel rebars immersed in alkaline solutions simulating concrete pores, Electrochim. Acta 52 (2007) 7634-7641. https://doi.org/10.1016/j.electacta.2007.02.012.